Electronic supplementary information for

Distinct thermal runaway mechanisms of sulfide-based all-solid-state batteries

Xinyu Rui,[a] Dongsheng Ren,*[ab] Xiang Liu,*[c] Xiaodan Wang,[b] Kuangyu Wang,[d] Yao Lu,[a] Linwei Li,[e, f] Pengbo Wang,[g] Gaolong Zhu,[g] Yuqiong Mao,[a] Xuning Feng,[a] Languang Lu,[a] Hewu Wang,[a] and Minggao Ouyang[a]*

[a] School of Vehicle and Mobility, Tsinghua University, Beijing 100084, P. R. China.
[b] Institute of Nuclear and New Energy Technology, Tsinghua University, Beijing 100084, P. R. China.
[c] School of Material Science and Engineering, Beihang University, Beijing 100084, P. R. China.
[d] State Key Lab of New Ceramics and Fine Processing, Tsinghua University, Beijing 100084, P. R. China
[e] Rare Earth Functional Materials (Xiong'an) Innovation Center Co., Ltd., Xiong'an 071700, P. R. China.
[f] National Engineering Research Center for Rare Earth, GRINM Group Co., Ltd, Beijing 100084, P. R. China.
[g] Prof. Ouyang Minggao Academician Workstation, Sichuan new Energy Vehicle innovation Center, Sichuan, 644000, P. R. China

*Email: ouymg@tsinghua.edu.cn (M. O.); rends@tsinghua.edu.cn (D. R.); xiangliu@buaa.edu.cn (X. L.)

1. Materials and Methods

Inorganic solid-state electrolytes (SEs): The oxide SEs, including $Li_{1.3}Al_{0.3}Ti_{1.7}P_3O_{12}$ (LATP), $Li_{1.5}Al_{0.5}Ge_{1.5}P_3O_{12}$ (LAGP), $Li_7La_3Zr_2O_{12}$ (LLZO) and $Li_{0.33}La_{0.56}TiO_3$ (LLTO) were purchased from DX Time Technology Co., Ltd. The sulfide SEs of Li_3PS_4 (LPS3), $Li_7P_3S_{11}$ (LPS7), Li_6PS_5Cl (LPSC) and $Li_{10}GeP_2S_{12}$ (LGPS) were purchased from Ganfeng LiEnergy Technology Co., Ltd. Note that the above LPS3 and LPS7 were glassy-ceramic SEs, while LPSC and LGPS have good crystallinity. To investigate the relationship between the thermal stabilities of sulfide SEs against NCM and their crystal structure, SEs with the same composition but different crystal structures were prepared. Crystalline LPS3 (γ-LPS3) was synthesized by ball milling and annealing. Glassy-ceramic LPSC (gc-LPSC) was provided by Grinm Group Co. Ltd.

Preparation of γ-LPS3: Li_2S (>99.9% purity) and P_2S_5 (>99.9% purity) (3: 1 mol%) were mixed in a zirconium jar with ZrO_2 balls in an argon-filled glove box. The mixture was ball milled at 350 rpm for 10 hours. The obtained powder was uniaxially pressed at 360 MPa into a pellet. After that, the pellet was sealed in a quartz tube and sintered at 510ºC for 2 hours in a muffle furnace. The XRD results of γ-LPS3 was shown in **Fig. S15**.

Liquid electrolyte: Commercial electrolyte with 1.0 M $LiPF_6$ in EC: DEC: EMC= 1: 1: 1 vol% was purchased from DoDoChem.

Preparation of active materials: The cathode and anode materials were obtained from a fully charged pouch cell with a capacity of 6 Ah. The pouch cell was charged to 4.2V with constant current and constant voltage (CC-CV) strategy and discharged to 3V with CC strategy at 1/3 C (2A) for three cycles. After the three cycles, the pouch cell was CC-CV charged to 4.2V (100% SOC) and then disassembled in the glove box to collect the active materials. The electrolyte used in the cell was 1.0 M $LiPF_6$ in EC: DEC: EMC= 1: 1: 1 vol%. To avoid residual impurities of electrodes, the charged electrodes were soaked and washed cleanly using dimethyl carbonate (DMC, purchased from Anhui Zesheng Technology Co., Ltd) and dried out in the argon atmosphere. Finally, the delithiated cathode and lithiated anode materials powder were scraped gently from the current collector and collected for subsequent tests. For cathode, the detailed compositions were $LiNi_{0.8}Co_{0.1}Mn_{0.1}O_2$: PVDF: carbon black = 97: 1.2: 1.8 wt%. For anode, the detailed compositions were graphite: CMC: SBR: black = 95.9: 1.3: 2.3: 1.8 wt%.

DSC-MS analysis: The thermal stability of various electrolytes and their mixtures with active materials were investigated by DSC 214 Polyma and STA449F5-QMS403D (NETZSCH, Germany). Inorganic solid electrolytes, including four oxides and four sulfides, were mixed with Ni-rich cathode materials in the DSC tests (**Table S1**). However, DSC-MS tests were only performed for sulfides + NCM samples because of their significant exothermic peaks in DSC profiles. The powder samples were sealed into the aluminum crucibles with pierced lid (30μL, NETZSCH, Germany) in the glove box. The weight ratio of active materials and electrolytes was set as NCM: Electrolytes = 2: 1. To ensure homogeneous mixing, the sealed crucibles were thoroughly mixed by hand shaking

before DSC-MS tests. The tests were conducted from 50 ºC to 550 ℃ at a scanning rate of 10 ℃·min^{-1} with N_2 (DSC) or Ar (DSC-MS) atmosphere. For the MS spectra, the m/z =32 and 64 were detected, referring to O_2 and SO_2, respectively.

In order to qualitatively compare the amount of O_2 and SO_2 in different DSC-MS tests, it is necessary to ensure a similar sample mass and revise the intensity of the concerned gas according to the ion current intensity of carrier gas (Ar, m/z = 40) in those tests. The mass records are shown in **Table S2**, and the mass spectrums of Ar in STA-MS tests are illustrated in **Fig. S6**. Based on the result of LPSC+NCM, the correction coefficients were calculated as 0.989 (LGPS+NCM), 0.928 (LPS3+NCM), 0.914 (LPS7+NCM) and 1.133 (NCM), as listed in the **Table S2**.

DSC-MS experiments were also utilized to verify the proposed two different failure modes. For the DSC–MS tests of sulfide SEs with O_2, O_2 with 99.9% purity was used to replace the original argon carrier gas in the STA449F4 equipment. During each experiment, the gas flow of O_2 was set as 50 ml/min, and the mass of sulfide SEs was 2 mg–4 mg. For the DSC tests of sulfide SEs with NiO, their weight ratio was around 3 mg : 3 mg. The scanning rates of temperature were 10 ℃·min^{-1} in the above experiments.

Configuration of rapid heating tests: The combustion phenomenon of composite cathode pellets was observed by rapid heating tests. The fully charged NCM powder was mixed with sulfide SEs uniformly by stirring at a 2:1 weight ratio. The powder mixtures were then poured into the die with a diameter of 4 mm, and pressed under 680 MPa to form pellets using a tablet press machine. All the above procedures were carried out in the glove box with argon atmosphere. The rapid heating tests were conducted not only in the fume hood but also in the glove box. Before being transferred to the fume hood, the pellet samples were protected from moist air by Kapton tape. The pellets were tightly attached to the heating plate, and a K−type thermocouple connected to the HIOKI data logger was used to detect the temperature near the pellets. The heating tests of NCM alone in the fume hood and LPS7 + NCM in glove box without Kapton were also performed for comparison, as shown in **Video S5** and **S6.**

Scanning Electron Microscopy (SEM): Microstructure images and elements mapping of the composites at different temperatures were obtained on a Merlin high−resolution scanning electron microscope (Carl Zeiss AG, Germany). A transfer shuttle was used to avoid air exposure of sulfide SEs.

X-ray Photoelectron Spectroscopy (XPS): XPS analysis was employed to confirm reaction products during elevated temperatures. XPS measurements were carried out using an ESCALAB Xi+ (Thermofisher Scientific, America) with monochromatized Al Kα X-ray source. All samples were transferred from an Ar−filled glovebox to the XPS instrument using a transfer vessel to avoid air exposure. The C 1s signal from adventitious hydrocarbons was set to 284.8 eV to correct for charging effects, and the Avantage software was used for the data analysis.

X-ray diffraction (XRD): The crystalline phases and structures of samples were identified by D8 Advance (Bruker, Germany) with Cu−Kα radiation in a 2θ range of 10º ~ 90º at 2º·min^{-1}. Kapton tape was used to seal the sample to avoid oxygen and water contamination.

Raman spectroscopy: Raman analysis of post-mortem samples was performed on LabRAM HR Evolution (HORIBA Jobin Yvon, Japan) at the excitation wavelength of 532nm with a 50X objective. To avoid air exposure, the samples at different temperatures were covered by two thin coverslips and sealed by parafilm in the glovebox before tests.

2. Supplementary Figures and Tables

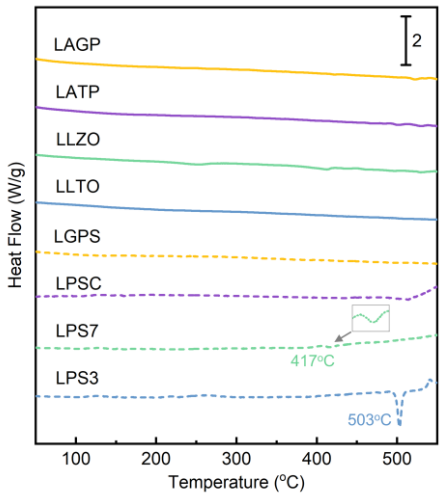

Fig. S1 DSC results of the inorganic SEs.

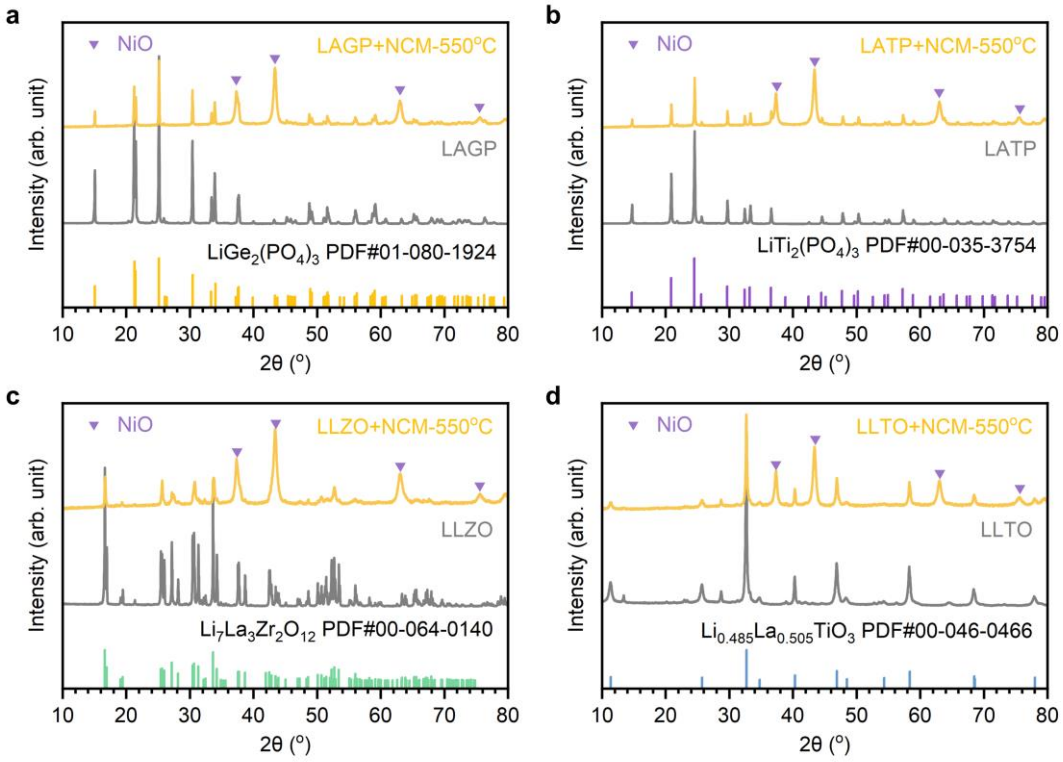

Fig. S2 XRD results of four oxide SEs and its mixture with NCM after being heated at 550°C. (a) LAGP, (b) LATP, (c) LLZO, (d) LLTO. The diffraction peaks of four oxide SEs remained unchanged with NCM cathode at 550°C, indicating excellent thermal stabilities of oxide SEs and NCM. PDF references for LAGP, LATP, and LLTO can be found in the literature. [1-3]

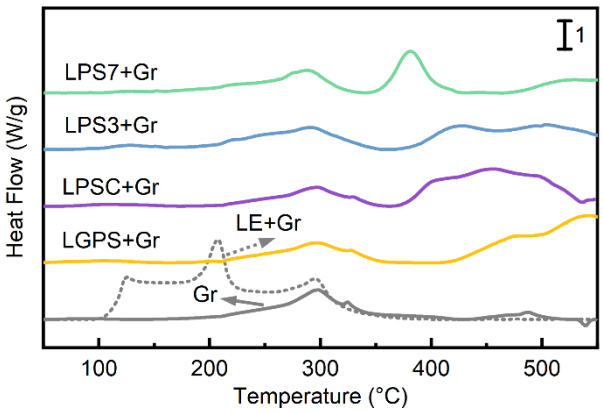

Fig. S3 DSC profiles of sulfide SEs + Gr, LE + Gr, and Gr alone. (Gr represents the fully lithiated graphite anode).

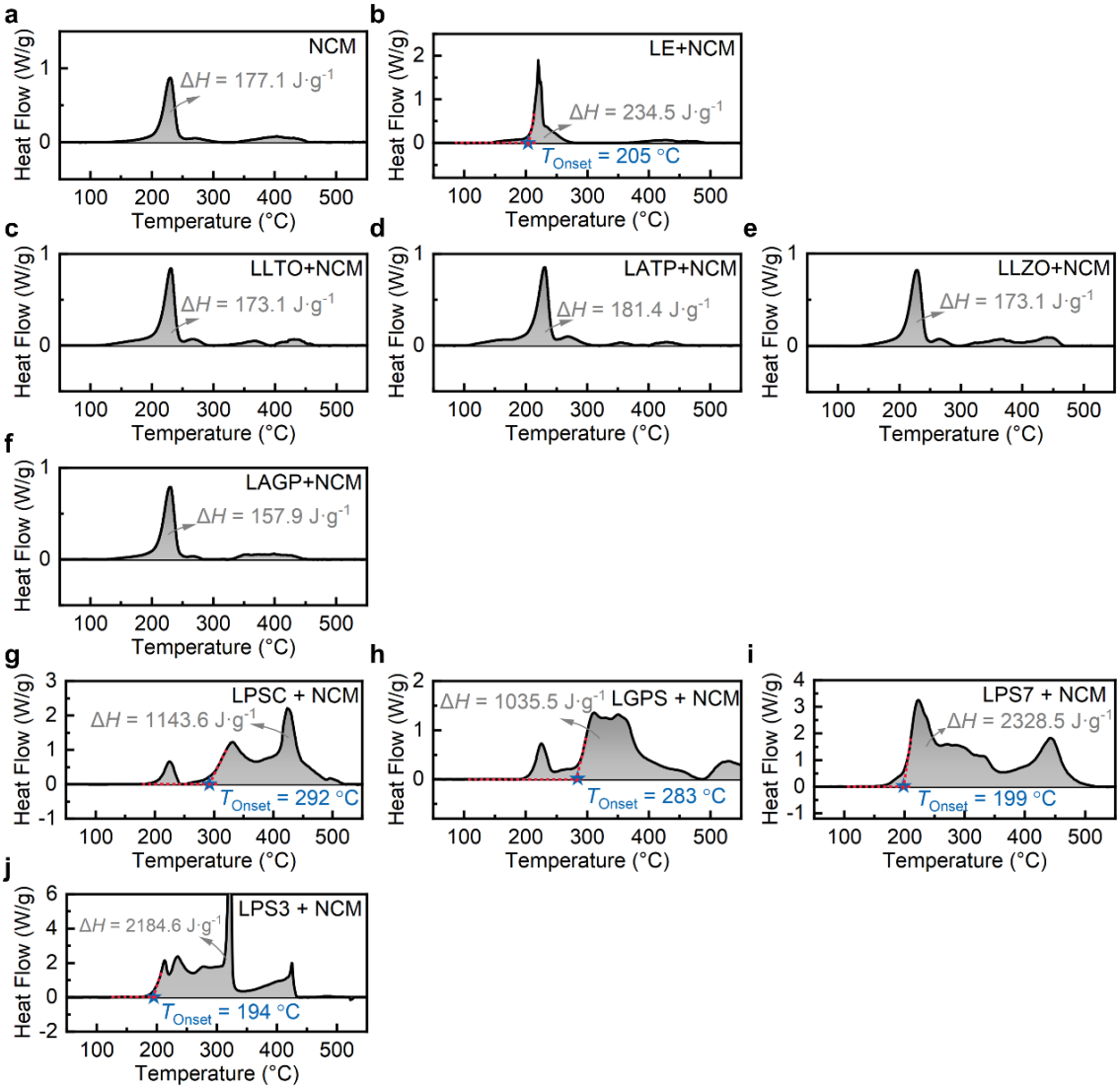

Fig. S4 The determination diagram of total heat release (ΔH) and onset temperature (T_{Onset}) of the first exothermic reation in various DSC experiments. To better compare the thermal stability of different electrolytes, the heat generation was normalized by the weight of the NCM powder in each composition.

Table S1 Key DSC test parameters, including the material composition, their mass ratio, and the results obtained from **Fig. S4**.

Sample No.	Composition	Mass (mg)	T_{Onset} (°C)	ΔH (J g^{-1})
1	NCM	3	——	177.1
2	LE + NCM	2.6 (μL) + 6.1 (mg)	205	234.5
3	LLTO + NCM	1.5 + 2.9	——	173.1
4	LATP + NCM	1.7 + 3.3	——	181.4
5	LLZO + NCM	1.8 + 3.7	——	173.1
6	LAGP + NCM	1.7 +3.2	——	157.9
7	LPSC + NCM	1.5 + 3.3	292	1143.6
8	LGPS + NCM	1.4 + 3	283	1035.5
9	LPS7311 + NCM	1.5 + 3.1	199	2328.5
10	LPS314 + NCM	1.6 + 2.9	194	2184.6

Table S2 The masses of sulfide SEs + NCM samples in DSC−MS measurements.

Sample No.	Composition	Mass	Correction factor
1	LPSC + NCM	2.1 mg + 4.4 mg	1
2	LGPS + NCM	2.1 mg + 4.1 mg	0.989
3	LPS3 + NCM	2.1 mg + 4.1 mg	0.928
4	LPS7 + NCM	2 mg + 4.1mg	0.914
5	NCM	4.2 mg	1.133

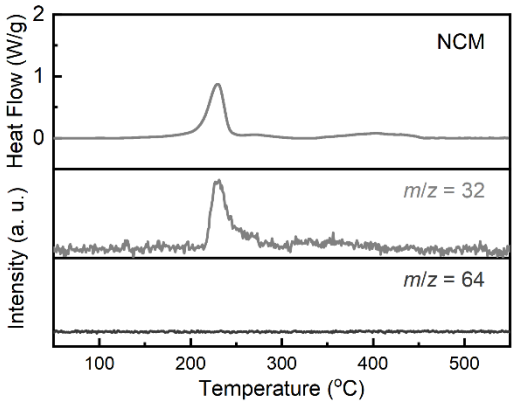

Fig. S5 DSC-MS profiles of fully charged NCM cathode materials from 50 °C to 550 °C. According to the MS spectra, the NCM cathode generated large amounts of O_2 with m/z = 32, indicating phase transformation from layered to spinel structure. Compared to NCM with sulfide SEs, there was no SO_2 observed in the DSC−MS test of the NCM sample.

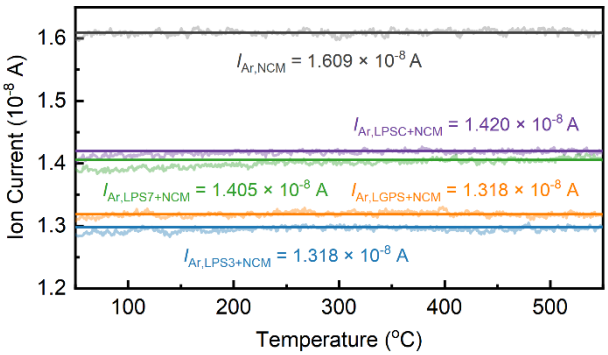

Fig. S6 The mass spectrums of Ar and their average values for determining correction coefficients in various DSC−MS tests.

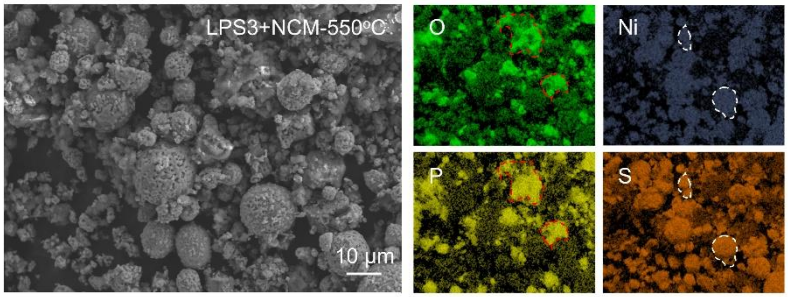

Fig. S7 SEM and EDS results of LPS3 + NCM at 550 °C.

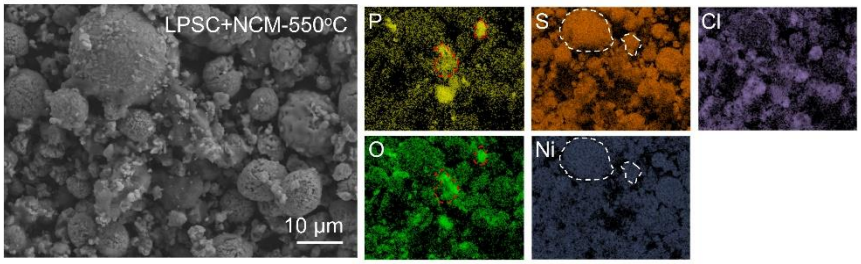

Fig. S8 SEM and EDS results of LPSC + NCM at 550 °C.

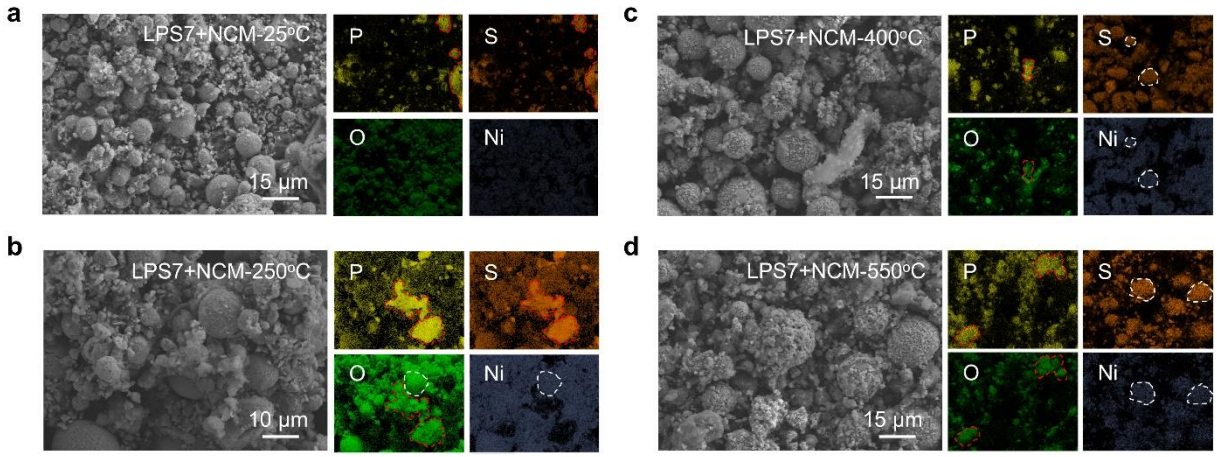

Fig. S9 SEM and EDS results of LPS7 + NCM at (a) 25 °C, (b) 250 °C, (c) 400 °C, and (d) 550 °C.

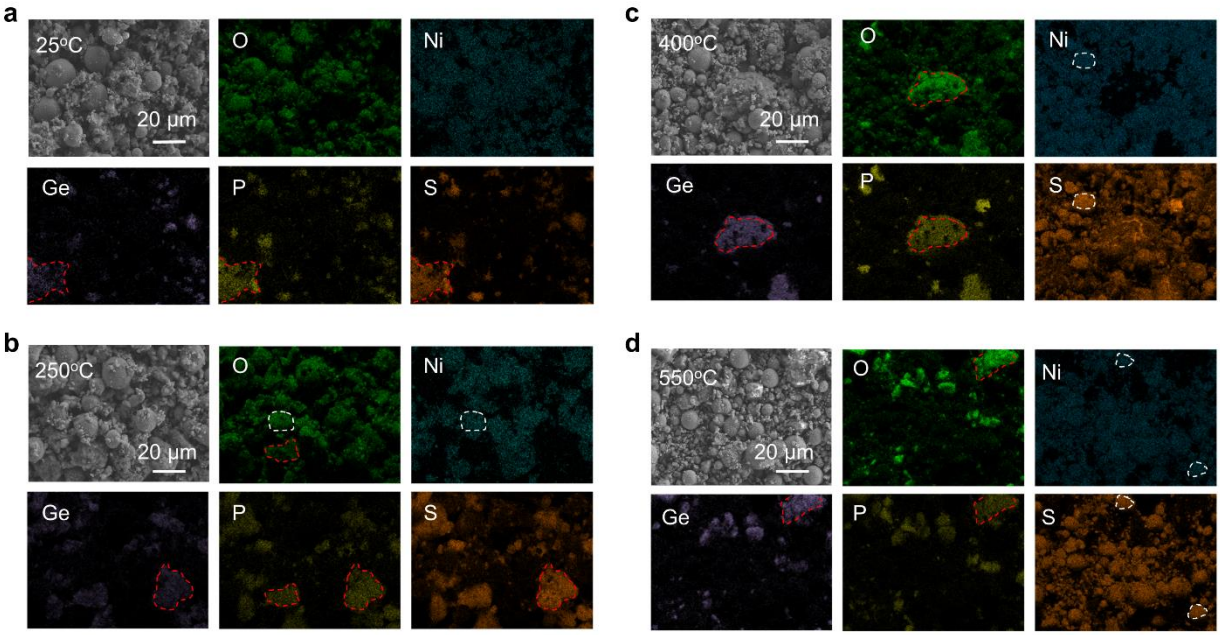

Fig. S10 SEM and EDS results of LGPS + NCM at (a) 25 °C, (b) 250 °C, (c) 400 °C, and (d) 550 °C.

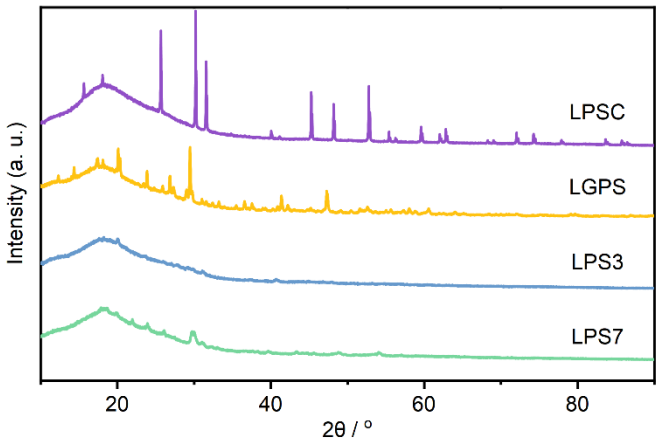

Fig. S11 XRD patterns of four sulfide SEs at pristine states.

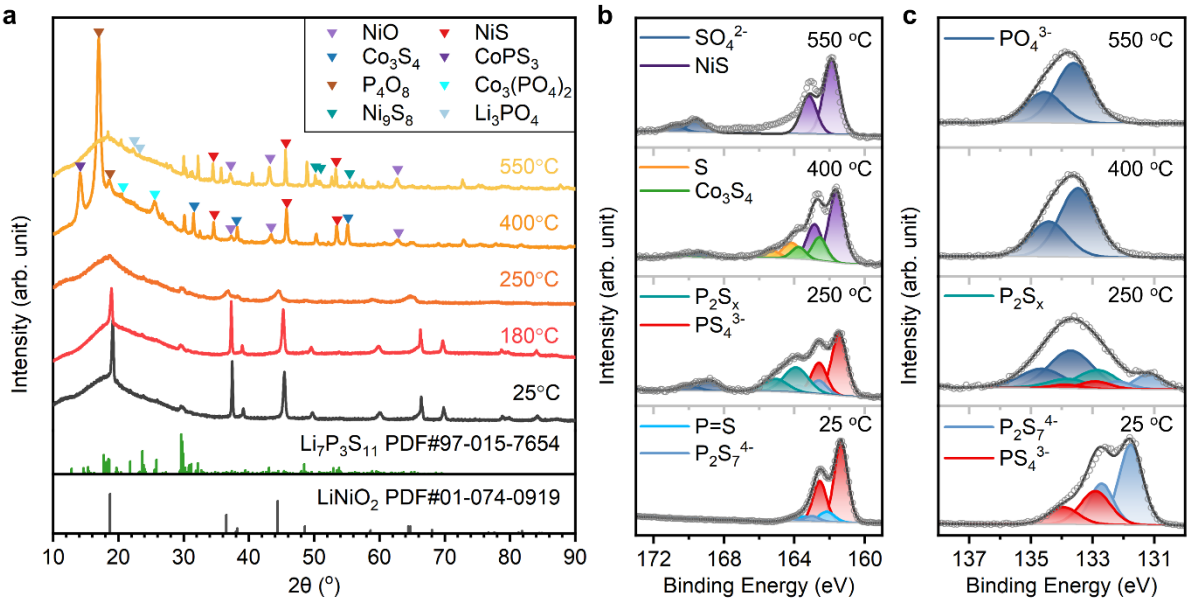

Fig. S12 *Ex situ* characterization of LPS7 + NCM samples at different temperatures. (a) XRD results. (b) –(c) XPS spectra and their fitting results: (b) S 2p; (c) P 2p.

The XRD and XPS results of LPS7 + NCM at high temperatures are summarized in **Fig. S12**. Similar to LPS3, LPS7 also had a much lower degree of crystallinity than NCM, and only faint peaks of LPS7 near 30° were visible in the XRD results of composite samples at 25 °C, 180 °C, and 250 °C (**Fig. S12**a). When the temperature arrived at 250 °C, the diffraction peaks of NCM changed significantly, indicating that it has undergone transformation. It could not distinguish the evolution of LPS7 at 250 °C from XRD observations due to the relatively low intensity. However, XPS spectra afforded strong evidence for gas-solid reaction (GSR) near 200 °C. The pristine LPS7 composed of PS_4^{3-} and $P_2S_7^{4-}$ units were obtained with the peak of 132.9 eV and 131.8 eV in P 2p signal, respectively. However, there were three different sulfur species: one bridging ($P_2S_7^{4-}$, ~163 eV), three double bound (PS, 162.1 eV) and seven P-S-Li sulfur atoms (PS_4^{3-}, 161.3 eV) in LPS7.[4] With the temperature reached 250 °C, the XPS spectra of S 2p and P 2p became significantly broader and more complex than that of the pristine LPS7. The signal of S 2p was deconvolved into SO_4^{2-}, P_2S_x,

$P_2S_7^{4-}$ and PS_4^{3-} groups. Apart from the same components in S 2p, a high intensity peak of PO_4^{3-} was detected in P 2p at 250 °C. Substantial phosphates indicated a chemical reaction between LPS7 and NCM through GSR pathway, which is consistent with the descriptions of LPS3 in the main text. For the LPS7 + NCM at 400 °C, the products detected by XRD were $CoPS_3$, P_4O_8, $Co_3(PO_4)_2$, Co_3S_4, NiS and NiO. On the other hand, PS_4^{3-}, $P_2S_7^{4-}$ and P_2S_x groups disappeared in the XPS spectra at 400 °C. The major peaks of NiS, Co_3S_4 and PO_4^{3-} verified the XRD analysis at the same temperature. Additionally, elemental sulfur (164 eV) was detected in the spectra of S 2p. When the temperature exceeded 550 °C, different impurities was found in XRD diffraction peaks, involving Li_3PO_4, NiS, NiO and Ni_9S_8. Correspondingly, the XPS curves mainly fitted with SO_4^{2-}, NiS and PO_4^{3-}. Overall, the evolution process of LPS7 + NCM under high temperatures was close to the LPS3 + NCM with the GSR failure mode.

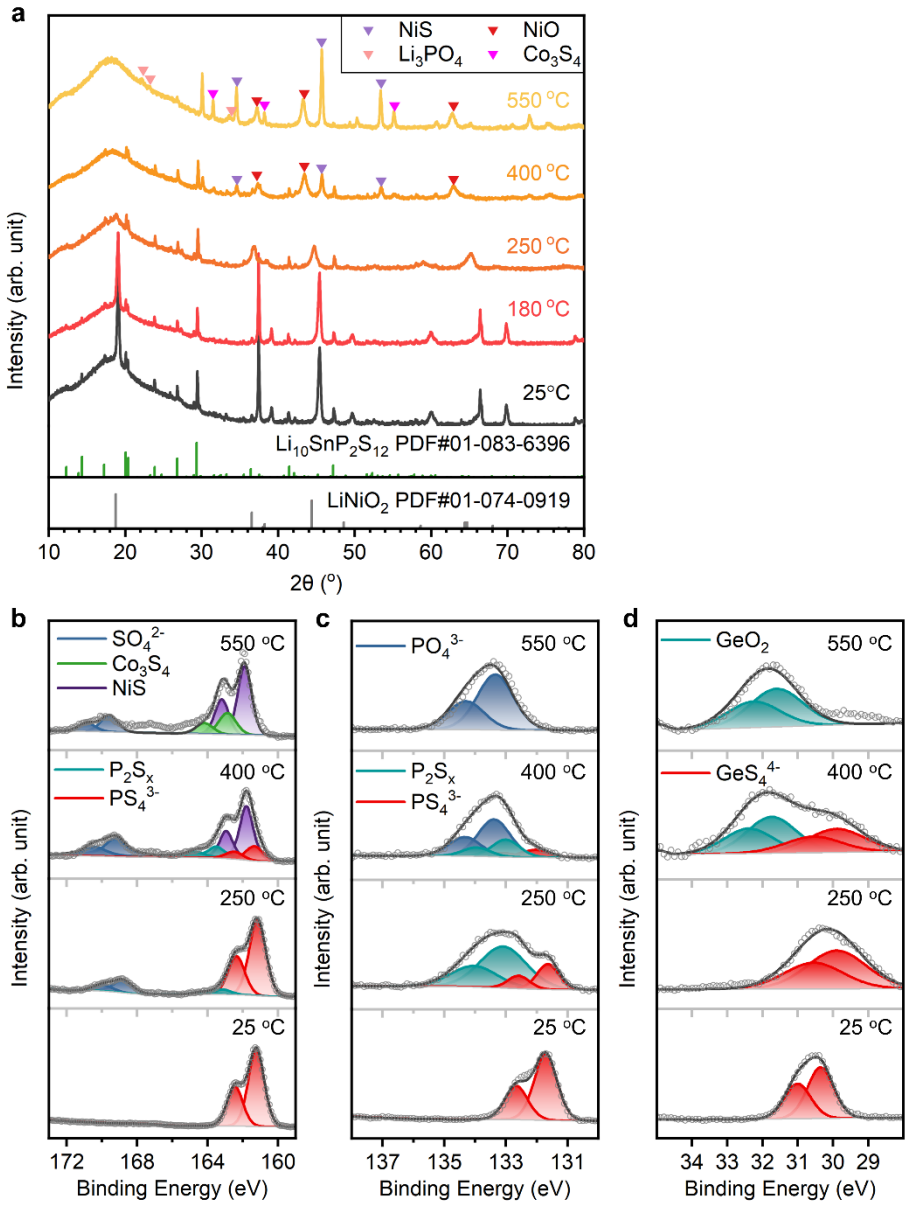

Fig. S13 *Ex situ* characterization of LGPS + NCM samples at different temperatures. (a)XRD results. (b)–(d) XPS spectra and their fitting results: (b) S 2p; (c) P 2p; (d) Ge 3d. LGPS has the same structure as $Li_{10}SnP_2S_{12}$ (LSPS), so the main peaks of LGPS correspond to the peaks of LSPS standard card (PDF#01-083-6396).[5]

The XRD and XPS results of LGPS+NCM at high temperatures are summarized in **Fig. S13**. Comparing the XRD patterns of the reaction products at different temperatures (**Fig. S13**a), it could be found that the main peaks of LGPS still maintained at 250 °C. According to the XPS results of S 2p (**Fig. S13**b) and P 2p (**Fig. S13**c), a slight interfacial reaction between LGPS and NCM has formed SO_4^{2-} and P_2S_x. When the temperature reached 400 °C, obvious impurities of NiS and NiO appeared in the XRD patterns. In the XPS spectra at 400 °C, the S 2p results could be deconvolved into SO_4^{2-}, P_2S_x, NiS, and PS_4^{3-}; and P 2p curve was fitted with P_2S_x, PO_4^{3-}, and PS_4^{3-}. GeO_2 with a peak of ~31.74 eV in Ge 3d was also observed (**Fig. S13**d).[6] When the temperature was further increased to 550 °C, NiS, NiO, Co_3S_4, and Li_3PO_4 impurities were found in XRD patterns. On the other hand, comparing the XPS analysis at 400 °C and 550 °C, the pristine groups of LGPS (PS_4^{3-}

and GeS_4^{4-}) and P_2S_x disappeared. The fitting results of S 2p and P 2p at 550 °C showed the groups of SO_4^{2-}, NiS, Co_3S_4, and PO_4^{3-}, echoing the detections in XRD patterns. Similar features of product evolution with LPSC + NCM samples suggested that LGPS reacts with NCM also belongs to the solid-solid reaction (SSR) failure route.

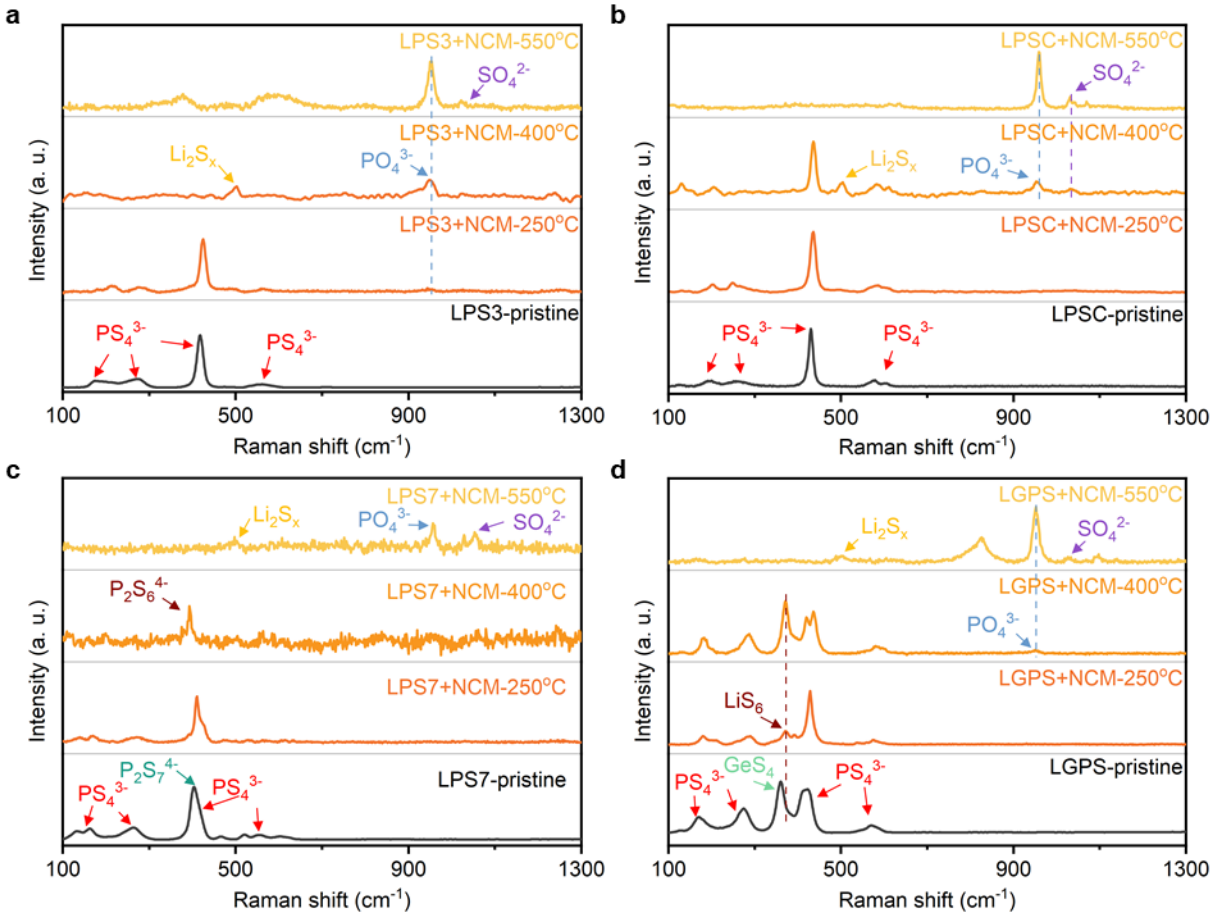

Fig. S14 Raman spectra of (a) LPS3, (b) LPSC, (c) LPS7, (d) LGPS with NCM cathode at different temperatures.

At pristine state, LPS3, LPSC, LGP7, and LGPS exhibited five characteristic peaks at around 195, 272, 425, 573, and 600 cm^{-1}, referring the PS_4^{3-} tetrahedral unit.[7] In addition to PS_4^{3-}, LPS7 contained a $P_2S_7^{4-}$ group at 405cm^{-1},[8] while LGPS had GeS_4 and LiS_6 units at approximately 360 and 372cm^{-1}, respectively.[9, 10] In LPS3+NCM mixtures, the PS_4^{3-} remained unchanged after heating at 250°C, but disappeared as the heating temperature increased to 400°C, along with the generation of PO_4^{3-} (950 cm^{-1}) [11] and Li_2S_x (495 cm^{-1}).[12] At 550°C, the weak peak of SO_4^{2-} ions attributed to Li_2SO_4 products was observed near 1010 cm^{-1}.[13] Similarly, the spectra of LPSC showed the oxidation products of PO_4^{3-} and SO_4^{2-} at 400 and 550°C. However, the PS_4^{3-} unit was still observed in the spectra of LPSC at 400°C, indicating the better thermal stability of LPSC than LPS3 against NCM.

For LPS7, when the heating temperature increased to 400°C, the original PS_4^{3-} and $P_2S_7^{4-}$ unit

disappeared, and a new peak at around 390 cm^{-1} emerged. The peak near 390cm^{-1} may refer to the $P_2S_6^{4-}$,[14] generated from the oxidation of metastable phase $P_2S_7^{4-}$. Similarly, $PO_4^{3-}$and SO_4^{2-} were found in LPS7+NCM at 550°C. For LGPS, the GeS_4 unit disappeared after heating at 250°C, and PO_4^{3-} at 950cm^{-1} was observed after heating at 400°C and became the dominant product at 550°C. Moreover, SO_4^{2-} and Li_2S_x can also be found at the heating temperature of 550°C.

The detection of sulfates (SO_4^{2-}) and phosphates (PO_4^{3-}) in the Raman spectra of four sulfide SEs + NCM at 400-550°C confirmed the XPS and XRD results. Furthermore, the identification of Li_2S_x in the Raman spectra helped to complement the findings of the XRD and XPS tests.

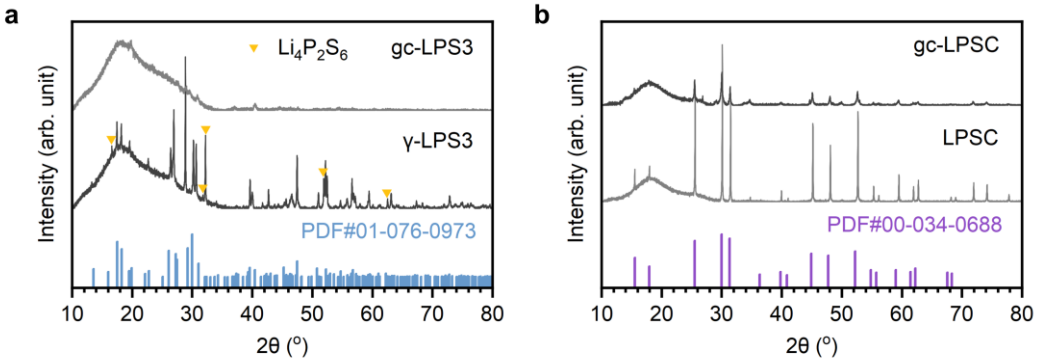

Fig. S15 XRD comparison of (a) γ-LPS3 and gc-LPS3, (b) gc-LPSC and LPSC. The prepared γ-LPS3 sulfide SE has much better crystallinity than the gc-LPS3. However, there existed some impurities like $Li_4P_2S_6$ in γ-LPS3, which could not be eliminated by the optimization of the synthesis process in a limited time. For the gc-LPSC, broadened peaks with low intensity can be observed in gc-LPSC (**Fig. S15**b). Nevertheless, there is still a gap between the obtained gc-LPSC SEs and the ideal glass-ceramic argyrodites.

Table S3 Detailed information of DSC-MS tests for investigating the relationship between thermal stabilities of sulfide SEs with NCM and their crystallinity.

Composition	Mass	Average I_{Ar}	Correction factor	
γ-LPS3 + NCM	1.9 mg + 4.0 mg	6.404×10^{-8}A	1/4.86	New
gc-LPS3 + NCM	2.1 mg + 4.1 mg	1.318×10^{-8}A	1	**Table S2**
gc-LPSC + NCM	2.0 mg + 4.2 mg	2.014×10^{-7}A	1/14.2	New
LPSC + NCM	2.1 mg + 4.4 mg	1.420×10^{-8}A	1	**Table S2**

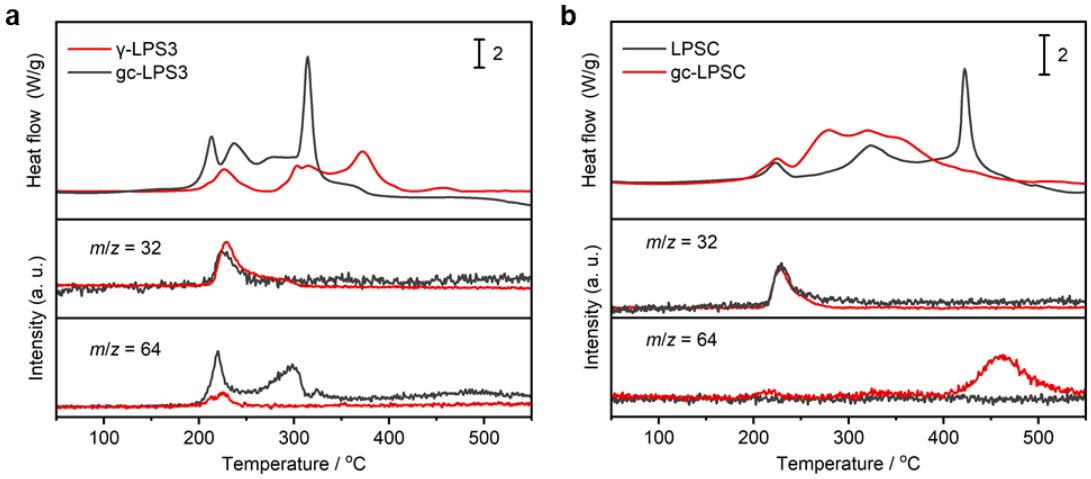

Fig. S16 Exothermic behaviors and gas evolution of (a) γ-LPS3/gc-LPS3 (b) LPSC/gc-LPSC with NCM. m/z = 32 and 64 represent the gaseous O_2 and SO_2, respectively.

In order to qualitatively compare the amounts of gaseous products in above two DSC-MS tests, keeping a similar sample mass and calculating the correction factors according to the ion current intensity of carrier gas (Ar, m/z = 40) were necessary. The mass record and correction factors were displayed in **Table S3**. The DSC results are shown in **Fig. S16**. The crystalline γ-LPS3 showed better thermal stability against NCM materials, as the first exothermic peak shifted to a higher temperature (226°C) compared to gc-LPS3 (213.5°C). The intensity of the first exothermic peak of γ-LPS3 with NCM was also much lower than that of gc-LPS3. Moreover, the intensity of SO_2 spectra (m/z=64) from γ-LPS3 decreased significantly at around 200°C, accompanied by an increase in O_2 generation. Based on the DSC-MS results, the reactivity of crystalline γ-LPS3 with the O_2 released from the NCM cathode decreases significantly, and the thermal failure of γ-LPS3 with the NCM cathode seems to follow the SSR mechanism at higher temperatures. On the contrary, the gc-LPSC reacted with NCM more intensely than LPSC (**Fig. S16**b). The first exothermic peak of gc-LPSC + NCM became stronger than LPSC+NCM, companies with a tiny amount of SO_2. The characteristics of gc-LPSC were similar to glassy-ceramic SEs LPS3 and LPS7, in which thermal failures were triggered by GSR near 200°C.

3. DSC-TG-MS tests on sulfide composite cathodes in mold-type all-solid-state batteries (ASSBs)

In this study, delithiated NCM cathode materials were obtained from a fully charged pouch cell with LE (***Materials and Methods*** in ESI). Indeed, the cathode active materials charged in the SEs and Les-based batteries might be slightly different. For the cathode charged in LEs-based batteries, a nanoscale cathode electrolyte interface (CEI) layer was formed during the initial charging and discharging process, consisting of LiF, Li_2CO_3, Li_2O and some other organic species as reported in previous research.[15] The CEI layer of the charged cathode in ASSBs may be different due to the different interfacial reaction mechanisms. However, despite surface differences, the major bulk phase of the high-nickel cathode materials is the same with a similar delithiation state. Recently, Charbonnel et al. investigated the TR mechanisms of ASSBs, which are obtained from LEs-based battery. They washed the LEs-based battery cleanly by DMC and reconstituted it with SEs, which effectively demonstrated the significance of this methodology for the safety evaluation of ASSBs.[16]

To further illustrate the feasibility and effectiveness of the proposed method for obtaining NCM in probing the failure mechanism in ASSBs, DSC-TG-MS tests were also performed on sulfide composite cathodes that were charged in ASSBs without the presence of LEs. Considerable efforts have been devoted to the preparation of sulfide-based ASSBs, the development of cathode material separation techniques from ASSBs, and the investigation of their impact on thermal failure behaviors. Although the obtained high-nickel cathode materials from ASSBs may not have been perfect, the DSC-TG-MS test results once again proved the two distinct failure routes for LPS3 and LPSC against high-nickel cathodes, which aligned with the proposed mechanisms in the manuscript (GSR and SSR failure modes). The detailed experimental procedure and analysis are presented following.

3.1 Preparation of mold-type sulfide-based ASSBs and their electrochemical performance

Sulfide-based Ni83|LPSC|Li-In ASSBs were assembled, as shown in **Fig. S17**a. To prepare the composite cathode mixture, $LiNi_{0.83}Co_{0.11}Mn_{0.06}O_2$ (Ni83, provided by a third party), the solid-state electrolyte (LPSC, Ganfeng LiEnergy Technology Co., Ltd) and the conductive agent (VGCF, Guangdong Canrd New Energy Technology Co., Ltd.) were mixed in a weight ratio of 70:30:3. Afterwards, the mold-type ASSB was assembled by pressing the LPSC SE (85 mg) with 350 MPa for 2 minutes as an electrolyte layer. Next, the composite cathode mixture (10.5 mg) was added into the mold, and the composite cathode and the electrolyte layer were pressed together at 350 MPa for another 2 minutes. Lithium-indium alloy foil (Guangdong Canrd New Energy Technology Co., Ltd.) was attached to the opposite side, acting as a negative electrode. All assembly processes were conducted in a glove box ($[H_2O] < 0.01$ ppm, $[O_2] < 0.01$ ppm) with high-purity (99.999%) Ar. It is important to note that the glass-ceramic electrolytes LPS3 and LPS7, as well as crystalline LGPS mentioned in the manuscript, were not used in the ASSBs. This was due to their low Li^+ ion conductivity and the severe side reactions with the high-nickel cathode,[17-19] which are not conducive to the electrochemical performance of the ASSBs.

Three mold-type ASSBs were charged and discharged for one cycle and then fully charged before disassembling. The charge and discharge process was performed at 45 °C using a current rate of 0.05C and cut-off voltages ranging from 2.1 V to 3.7 V (vs. Li-In). The pressure applied on ASSBs during cycling was ~50 MPa by a stainless steel holder. **Fig. S17**b-d presented the voltage profiles of the three ASSBs. It is noteworthy that the Ni83 cathode exhibited a charge capacity of approximately 250 mAh g^{-1} and a discharge capacity of 210 mAh g^{-1}, and can be comparable with the delithiated NCM cathode utilized in the manuscript.

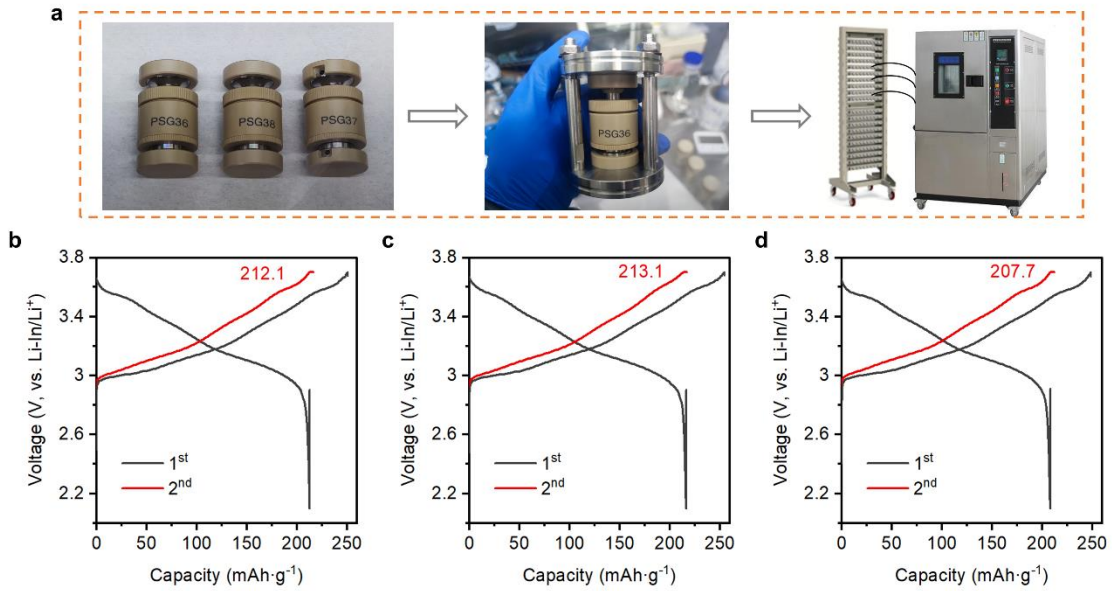

Fig. S17 (a) The preparation of charged mold-type sulfide-based ASSBs. (b)-(d) charge-discharge profiles of three mold-type ASSBs. The charge capacity of the second cycle was observed to be around 210 mAh g^{-1}, indicating the Ni83 cathode reached a nearly fully-charged state.

3.2 Separation techniques of cathode material from ASSBs and their impact on thermal failure behaviors of the cathode

After fully charged to 3.7 V, the three ASSBs were disassembled in the glove box, as depicted in **Fig. S18**a. However, obtaining the pure cathode active material from the highly condensed composite cathode is a challenging task, particularly when it came to separating the electrolytes mixed in the composite cathode. To address this issue, we have tried various approaches, including scratching and washing with different solvents such as ethyl alcohol, n-hexane, and dimethyl carbonate. Ultimately, washing by ethyl alcohol (GR, >99.8%) was chosen as the most effective method to obtain the charged Ni83, as shown in **Fig. S18**b-d. During the washing process using ethyl alcohol, the bulk of the ASSBs was soaked for a sufficient duration. Within this period, some of the LPSC dissolved into the alcohol, resulting in a noticeable color change in the solution. The cathode materials could be easily detached from the bulk during this process. Finally, the materials were thoroughly washed with fresh alcohol three times to ensure their cleanliness, followed by

vacuum processing to remove any residual alcohol.

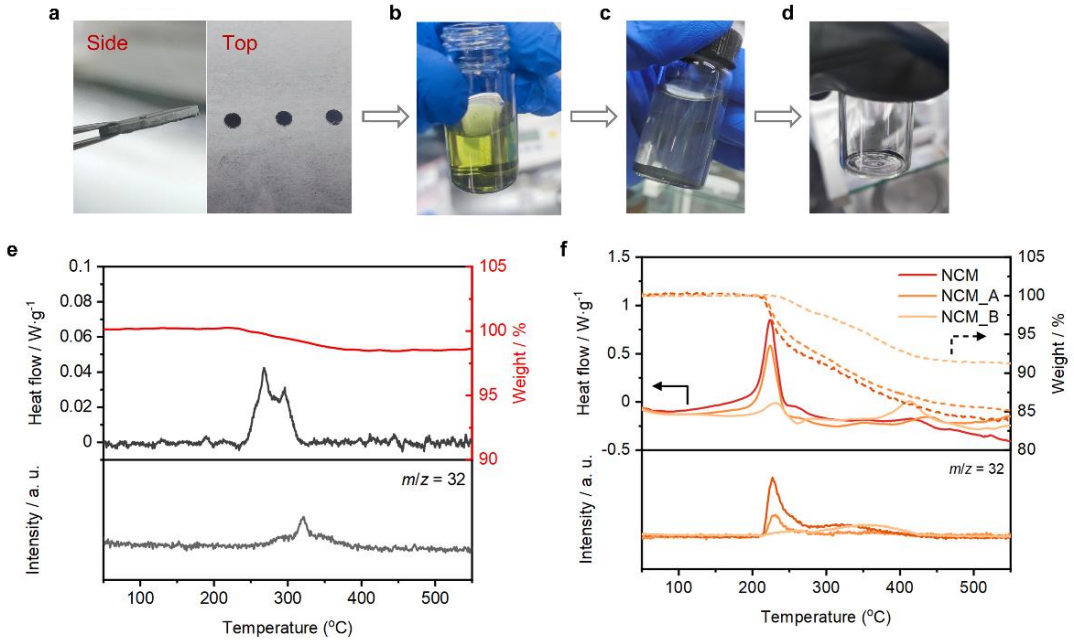

Fig. S18 (a) Bulk materials of ASSB, which consist of three compact layers—composite cathode layer, electrolyte layer and Li-In alloy foil layer. (b) soaking and (c) washing the ASSBs with ethyl alcohol to separate the Ni83 materials and SEs. (d) the final cathode materials after vacuum treatment. DSC-TG-MS profiles of (e) Ni83 after being washed by alcohol from ASSBs, (f) pristine NCM and NCM after being treated by different approaches. NCM_A denotes the NCM after being soaked in alcohol for 30 minutes and dried. The NCM_B sample was prepared by immersing the NCM in a LPSC-alcohol solution (~50 mL alcohol + 15 mg LPSC) for 30 minutes, followed by three washes of pure alcohol. The heat flow and the ion fragment with m/z = 32 showed that the alcohol solution dissolved with the sulfide SE has a significant effect on the thermal stability of delithiated high-nickel cathode.

To investigate the properties of Ni83 cathode material derived from charged ASSBs, DSC-TG-MS tests were first performed. Surprisingly, the heat generation of the Ni83 cathode material was very weak, with a peak heat flow of only 0.04 W g^{-1} at 267.5 °C. O_2 generation (m/z = 32) was observed in the range of 250-400°C for the charged Ni83 (**Fig. S18**e). This was striking, as the exothermic reaction and oxygen evolution of fully-charged Ni83 cathode material and fully-charged NCM (**Fig. S5**) are expected to be similar, occurring obviously at around 220 °C. The observed difference was likely due to the process of separating the Ni83 cathode material from ASSBs. Therefore, the effect of the soaking and washing process was studied using delithiated NCM, which was the same in the manuscript. **Fig. S18**f presented DSC-TG-MS profiles of delithiated NCM under different treatments, with NCM soaked in alcohol for 30 minutes and dried (NCM_A) and NCM immersed in a LPSC-alcohol solution (~50 mL alcohol + 15 mg LPSC) for 30 minutes followed by three washes of pure alcohol (NCM_B) used for comparison. Despite a slightly lower peak intensity and decreased O_2 generation of NCM_A, the temperature of the first exothermic peak remained constant (**Fig. S18**f). In contrast, NCM_B displayed a much milder thermal failure behavior, with the first peak shifting to a higher temperature at 231 °C and sharply reduced heat and O_2 generation (200-300 °C). It was speculated that the alcohol solution dissolved with LPSC may have left some

impurities on the surface of the NCM particles, affecting the thermal stability of the original NCM materials. Based on this, it was concluded that the alcohol solution dissolved with the sulfide SE has a significant effect on the delithiated high-nickel cathode, resulting in reduced heat production and O_2 evolution observed in the Ni83 test (**Fig. S18**e). However, a detailed explanation of this interesting phenomenon and the treatment improvement for cathode active materials were not further explored in this study. Nevertheless, the following experiments were carried out using the obtained Ni83 cathode.

3.3 DSC-TG-MS analysis on two types of sulfide SEs with charged Ni83 materials and the validation of proposed mechanisms

The DSC-TG-MS tests of LPS3 and LPSC with Ni83 were conducted to verify the two distinct failure routes of these SEs in ASSBs scenario, as shown in **Fig. S19**. The charged Ni83 was mixed well with the SEs in a 2:1 mass ratio, and all other test conditions were also consistent with those described in the ***Materials and methods***. In the Ni83+LPS3 sample, two continuous peaks were observed between 200-300°C temperature. The first exothermic peak of Ni83 with LPS3 shifted to 220 °C from the original peak (267.5 °C) observed in **Fig. S18**e. Furthermore, a spike at 325°C with a heat flow of 29.9 W g^{-1} was observed in the DSC profile of Ni83+ LPS3, indicating an intense reaction between LPS3 and charged Ni83. The intense signal of SO_2 (*m*/*z*=64) was also detected, during the exothermic reactions between 200-300 °C, indicating a reaction between LPS3 and the O_2 generated from Ni83 transformation. On the contrary, the first peak of Ni83+LPSC sample occurred at 255 °C and was almost identical to the exothermic peak of Ni83 (**Fig. S18**e). LPSC showed a faint peak of SO_2 near 314 °C, significantly higher than the temperature observed for Ni83+LPS3 sample. These observations suggested that LPSC exhibited better stability with O_2 at 200-300°C compared to LPS3. The thermal failure of LPSC was primarily attributed to the reactions between sulfide SE and transition-metal oxides generated, from the phase transformation of Ni83. Overall, the DSC-TG-MS results indicated that LPS3 mixed with charged Ni83 exhibited lower thermal stability compared to LPSC. This result aligned with the proposed mechanisms in the manuscript, which suggested that LPS3 experiences thermal failure induced by the gas-solid reactions (GSR) between O_2 and SE at lower temperatures, while LPSC failed through solid-solid reactions.

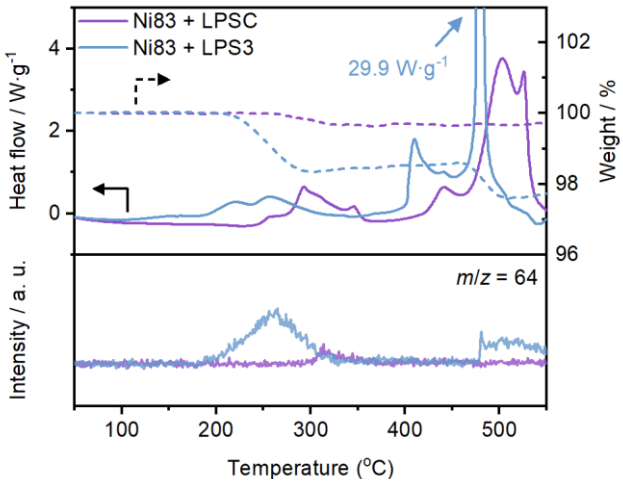

Fig. S19 DSC-TG-MS comparison of Ni83 with LPSC and LPS3. The ion fragment with m/z = 32 referring to the O_2 was paid closed attention.

4. Supplementary Videos

Video S1 Combustion phenomenon of LPS7 + NCM in fume hood.

Video S2 Combustion phenomenon of LPS3 + NCM8 in fume hood.

Video S3 Combustion phenomenon of LGPS + NCM in fume hood.

Video S4 Combustion phenomenon of LPSC + NCM in fume hood.

Video S5 Combustion phenomenon of NCM in fume hood.

Video S6 Combustion phenomenon of LPS7 + NCM in glove box.

References

1. Z. Huang, J. Li, L. Li, H. Xu, C. Han, M. Liu, J. Xiang, X. Shen and M. Jing, *Ceramics International*, 2022, **48**, 25949-25957.
2. X. Ban, W. Zhang, N. Chen and C. Sun, *The Journal of Physical Chemistry C*, 2018, **122**, 9852-9858.
3. Y. Deng, X. Xu, L. Zhang, F. Du, Q. Liu, J. Chen, K. Meng, Y. Wu, M. Yang and Y. Jiang, *Journal of Materials Science & Technology*, 2022, **128**, 142-147.
4. S. Wenzel, D. A. Weber, T. Leichtweiss, M. R. Busche, J. Sann and J. Janek, *Solid State Ionics*, 2016, **286**, 24-33.
5. Q. Wang, D. Liu, X. Ma, X. Zhou and Z. Lei, *ACS Appl Mater Interfaces*, 2022, **14**, 22225-22232.
6. C. Wang, X. Li, Y. Zhao, M. N. Banis, J. Liang, X. Li, Y. Sun, K. R. Adair, Q. Sun, Y. Liu, F. Zhao, S. Deng, X. Lin, R. Li, Y. Hu, T. K. Sham, H. Huang, L. Zhang, R. Yang, S. Lu and X. Sun, *Small Methods*, 2019, **3**, 1900261.
7. Y. Zhou, C. Doerrer, J. Kasemchainan, P. G. Bruce, M. Pasta and L. J. Hardwick, *Batteries & Supercaps*, 2020, **3**, 647-652.
8. R. Xu, X. Xia, Z. Yao, X.. Wang, C. Gu and J. Tu, *Electrochimica Acta*, 2016, **219**, 235-240.
9. X. Li, H. Guan, Z. Ma, M. Liang, D. Song, H. Zhang, X. Shi, C. Li, L. Jiao and L. Zhang, *Journal of Energy Chemistry*, 2020, **48**, 195-202.
10. K. Kim, J. Park, G. Jeong, J. S. Yu, Y. C. Kim, M. S. Park, W. Cho and R. Kanno, *ChemSusChem*, 2019, **12**, 2637-2643.
11. K. Takada, M. Osada, N. Ohta, T. Inada, A. Kajiyama, H. Sasaki, S. Kondo, M. Watanabe and T. Sasaki, *Solid State Ionics*, 2005, **176**, 2355-2359.
12. L. Sang, R. T. Haasch, A. A. Gewirth and R. G. Nuzzo, *Chemistry of Materials*, 2017, **29**, 3029-3037.
13. M. Tatsumisago, R. Takano, M. Nose, K. Nagao, A. Kato, A. Sakuda, K. Tadanaga and A. Hayashi, *Journal of the Ceramic Society of Japan*, 2017, **125**, 433-437.
14. R. C. Xu, X. H. Xia, Z. J. Yao, X. L. Wang, C. D. Gu and J. P. Tu, *Electrochimica Acta*, 2016, **219**, 235-240.
15. W. Li, A. Dolocan, P. Oh, H. Celio, S. Park, J. Cho and A. Manthiram, *Nat Commun*, 2017, **8**, 14589.
16. J. Charbonnel, N. Darmet, C. Deilhes, L. Broche, M. Reytier, P.-X. Thivel and R. Vincent, *ACS Applied Energy Materials*, 2022, **5**, 10862-10871.
17. Y. Zhu, X. He and Y. Mo, *ACS Appl Mater Interfaces*, 2015, **7**, 23685-23693.
18. W. Zhang, F. H. Richter, S. P. Culver, T. Leichtweiss, J. G. Lozano, C. Dietrich, P. G. Bruce, W. G. Zeier and J. Janek, *ACS Appl Mater Interfaces*, 2018, **10**, 22226-22236.
19. M. Cronau, M. Szabo, C. König, T. B. Wassermann and B. Roling, *ACS Energy Letters*, 2021, **6**, 3072-3077.